J Mater Sci (2011) 46:3574–3582
DOI 10.1007/s10853-011-5271-8

Structure and magnetic properties of $Ni_xZn_{1-x}Fe_2O_4$ thin films prepared through electrodeposition method

A. E. Saba · E. M. Elsayed · M. M. Moharam · M. M. Rashad · R. M. Abou-Shahba

Received: 5 October 2010 / Accepted: 11 January 2011 / Published online: 26 January 2011

Abstract Nanocrystalline nickel–zinc ferrites $Ni_xZn_{1-x}Fe_2O_4$ thin films have been studied and synthesized via electrodeposition–anodization process. Electrodeposited $(NiZn)Fe_2$ alloys were obtained from non-aqueous ethylene glycol sulphate bath. The formed alloys were electrochemically oxidized (anodized) in aqueous (1 M KOH) solution, at room temperature, to the corresponding hydroxides. The parameters controlling the current efficiency of the electrodeposition of $(NiZn)Fe_2$ alloys such as the bath composition and the current density were studied and optimized. The anodized $(NiZn)Fe_2$ alloy films were annealed in air at different temperatures ranging from 850 to 1000 °C for different times from 1 to 4 h. The change in the crystal structure, crystallite size, microstructure, and magnetic properties of the produced ferrites were investigated using X-ray diffraction patterns (XRD), scanning electron microscope (SEM) and vibrating sample magnetometer (VSM). The results revealed the formation of Ni–Zn ferrites thin films were formed. The crystallite sizes of the produced films were in the range between 32 and 81 nm. High saturation magnetization of 48.81 emu/g was achieved for $Ni_{0.5}Zn_{0.5}Fe_2O_4$ thin film produced after annealing the alloy at 850 °C for 4 h. The annealing process of the oxidized alloy anodization process was found to be first order reaction. The activation energy of the crystallization of Ni–Zn ferrite was found to be 62 KJ/mol.

A. E. Saba · E. M. Elsayed · M. M. Moharam ·
M. M. Rashad (✉)
Central Metallurgical Research and Development Institute
(CMRDI), P.O. Box 87, Helwan, Egypt
e-mail: rashad133@yahoo.com

R. M. Abou-Shahba
Chemistry Department, Faculty of Science (Girls),
Al-Azhar University, Cairo, Egypt

Introduction

Nickel–zinc ferrites with spinel crystal structure; provide a family of magnetic materials which has large magnetic permeability at high frequencies, electrical resistivity, mechanical hardness, chemical stability and reasonable cost. Accordingly, they have been extensively used in a variety of electronic devices mainly, TV sets, transformer, microwaves integrated non-reciprocal circuits, memory core devices, radio frequency coil, rod antennas, read–write heads for high-speed digital tape or disk recording and telecommunication applications field [1–6]. Furthermore, nickel–zinc ferrites are used for the catalysis applications [7].

Most soft ferrites in practical use have the composition $MOFe_2O_3$ (where M represents a divalent metal ion) and present in spinel system which can present either in one of two structures, the normal spinel (like zinc ferrites) in which metal ions M^{2+} are located in the tetrahedral sites, symmetrically surrounded by four oxygen ions, while the second (like nickel ferrites) half of Fe^{3+} ions are located in the tetrahedral positions, whereas the other half, along with all the Ni^{2+} ions, are in the octahedral spinel structure. A normal spinel can be described as $M^{2+}Fe_2{}^{3+}O_4$ and an inverse ferrite as Fe^{3+} $(M^{2+}, Fe^{3+})O_4$. Moreover, Ni–Zn ferrite is a material combined the normal and inverse spinels which have very important magnetic properties for applications above 1 MHz [8].

Different synthesis procedures have been intensively studied in recent years to produce Ni–Zn ferrites thin films with high homogeneity like spray pyrolysis [9], reverse micelles [10], cathodic electrophoretic deposition (EPD) [11]. Electrodeposition process is an interesting process for synthesis of ferrite films and powders. It is used previously in synthesis of zinc ferrites [12], cobalt ferrites [13], copper ferrites [13–15] and nickel ferrites [13, 16], CoNi–barium ferrite composite [17]. The process has many advantages compared with the other techniques, which include: (a) low temperature, (b) low cost of starting materials and equipment, (c) control of the microstructure and the composition of the film and morphology and (d) the ability to deposit a film on a complex surface [14]. To best of our knowledge, no published work were done on the synthesis of Ni–Zn ferrites thin film via electrodeposition–anodization process

The present study aims to prepare Ni–Zn ferrites by the electrodeposition method. Nickel sulphate, zinc sulphate and ferrous ammonium sulphate were used as source of cations forming the ferrite material. The electrolytic behaviour of each of these salts and in admixture was studied. The produced ferrite films were characterized by X-ray diffraction (XRD), scanning electron microscope (SEM) and vibrating sample magnetometer (VSM) techniques.

Experimental

The electrodeposition of (Ni–Zn)Fe_2 alloys were carried out from ethylene glycol electrolyte bath containing 0.1 M $NiSO_4$, 0.1 M $ZnSO_4$, 0.1 M $(NH_4)_2Fe(SO_4)_2$. All solutions were prepared, immediately before each experiment by dissolving the requisite amount of analytically grade metal sulphates in the ethylene glycol. 0.1 M citric acid solution is supposed as complexant which avoid the hydroxide precipitation and sodium chloride was added to the plating bath to increase its conductivity. The substrates used were copper, stainless steel and low carbon steel. Pure graphite rod was used as anode. The bath was stirred at 800 rpm.

Cyclic voltammetric (CV) tests were performed at room temperature using a conventional three-electrode cell, in which copper was used as working electrode, the auxiliary electrode was a graphite rod. The reference electrode used was a saturated mercurous sulphate electrode (MSE), $E = 650$ mV vs standard hydrogen electrode (SHE). The deposition potentials were determined from the polarization curves. Cyclic voltammograms (CVs) were performed with a computer-controlled potentiostat (Volta-lab 21).

Electrodeposition was carried out galvanostatically using constant currents ranging from 0.25 to 1 A. Apparent current densities were obtained by dividing applied current by macroscopic surface area of the deposit. The deposition conditions were optimized to get good quality of (Ni–Zn)Fe_2 alloy films with maximum thickness.

The alloy films were anodized using aqueous 1 M KOH. The anodization current density and time were optimized to get well adhered oxide films to the substrates. After anodization, the films were washed with distilled water and annealed after drying.

The crystalline phases in the different annealed ferrite samples were identified using XRD on a Brucker axis D8 diffractometer using the Cu Kα ($\lambda = 1.5406$ Å) radiation and secondary monochromator in the range 2θ from 20° to 80°. The ferrite particle morphologies were observed by scanning electron microscope (SEM (JSM-5400). The magnetic properties of the ferrites were measured at room temperature using a vibrating sample magnetometer VSM (9600-1 LDJ, USA) in a maximum applied field of 15 kOe. From the obtained hysteresis loops, the saturation magnetization M_s, remanence magnetization ratio M_r and coercivity H_c were determined.

Results and discussion

Cyclic voltammetry

Figure 1a–f showed the CV of 0.1 M of $ZnSO_4$, $NiSO_4$, $(NH_4)_2Fe(SO_4)_2$, Ni–Zn alloy, Ni–Fe alloy, Ni–Zn–Fe alloy in ethylene glycol, respectively. Voltammetric studies were performed within the range of 1 to −2 V using the copper electrode as a cathode and the scan rate (S.R.) of 10 mV/s.

The produced CV of $ZnSO_4$ in Fig. 1a was characterized by two cathodic peaks (C_1, C_2) and two anodic peaks (A_1, A_2). The cathodic peaks appeared at −0.2 and −0.9 V for peaks C_1 and C_2 were related to the electrodeposition of zinc into the active sites of the electrode surface that were not blocked by ethylene glycol and the electrodeposition of zinc into the active sites that were librated when the ethylene glycol molecules were desorbed from the surface of the copper electrode, respectively [18]. Moreover, the bulk deposition of Zn was also contributed to C_2. On switching the scan to the positive direction, anodic peaks A_1 and A_2 were appeared at −0.8 and −0.5 V, which were associated with the reoxidation of metallic zinc formed during the scan in the negative direction [18].

Figure 1b, c showed the CV of 0.1 M $NiSO_4$ and $(NH_4)_2Fe(SO_4)_2$, respectively. CV of $NiSO_4$ was characterized by cathodic peak $E = -0.5$ V, corresponding to the reduction of nickel ions to the metallic state whereas the $(NH_4)_2Fe(SO_4)_2$ showed the cathodic and anodic peaks at $E = -0.2$ V and −0.5 V assigned to the reduction of ferrous ion to metallic iron and the electrodissolution of deposited iron, respectively.

Figure 1d indicated the CV of Ni–Zn alloy which was characterized by the cathodic peak $E = -0.47$ V related to the co-deposition of Ni–Zn alloy [19]. However, the addition of Zn^{2+} to Ni^{2+} solution decreased the current density of the cathodic peak of Ni from −86 to −43 $\mu A/cm^2$ which can be explained on the inhibition of hydrogen reduction by the presence of Zn^{2+} [20]. Furthermore, the

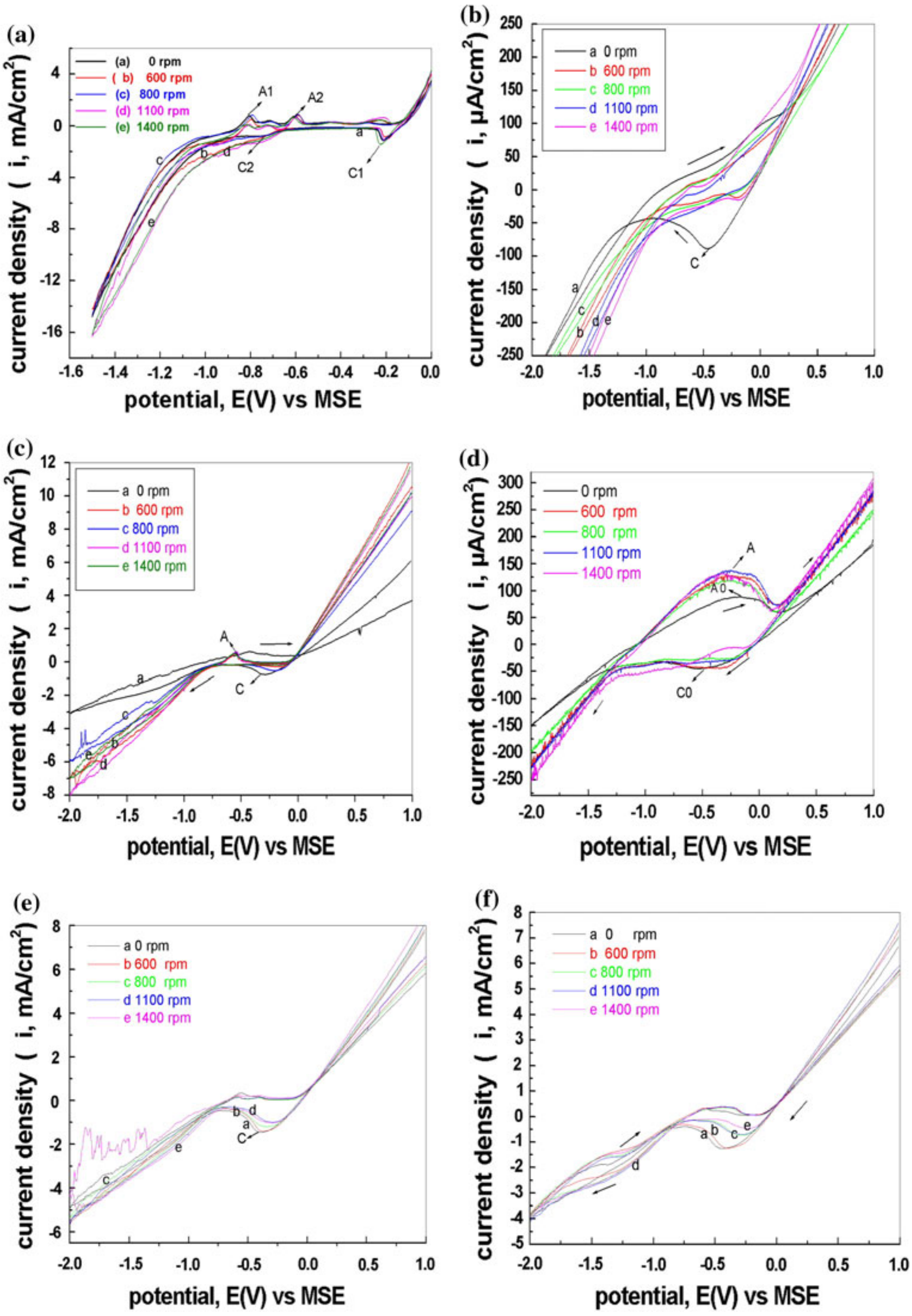

Fig. 1 Voltammograms obtained on Cu electrode in non-aqueous solution of **a** 0.1 M $ZnSO_4$, **b** $NiSO_4$, **c** $(NH_4)_2Fe(SO_4)_2$, **d** Ni–Zn alloy, **e** Ni–Fe alloy, **f** Ni–Zn–Fe alloy

anodic peak was appeared at ($E = -0.12$ V) which was corresponded to the electrodissolution of zinc-rich phase.

Figure 1e and f the CV of the electrodeposition Fe–Ni and Ni–Zn–Fe alloy which were characterized by the cathodic peaks at $E = -0.44$ V and $E = -0.47$ V, respectively. The peak supposed to be for the electrodeposition of Fe–Ni alloy [21]. Ni–Zn alloy and Fe–Ni alloy are considered as anomalous alloys [19, 21].

Chronoamperometric study

To study the mechanism of nucleation of electrochemical reaction, Scharifker and Hills [22] suggested model to describe the nucleation process during initial few seconds using chronoamperometric technique.

The nucleation process may be either progressive or instantaneous nucleation. Progressive nucleation corresponds to slow growth of nuclei on a less number of active sites, all of these sites activated at the same time. Instantaneous nucleation corresponds to fast growth of nuclei on many active sites, all activated during the course of electroreduction [22].

Figure 2 represents the potentiostatic current versus time (I–t) transients for nucleation and growth of (NiZn)Fe_2 alloy at different potentials ranging between 570 and 1400 mV

The transients were separated into three regions. The first region corresponds to short times ($t < 0.5$ s). In this region the decrease in the cathodic current density was related to the charging of a double layer. The second region relates to the crystal nucleation process and growth of the crystals formed during the first region. The third region was corresponded to the decline in the current density, which represented the diffusion process [18, 22, 23].

The transients have been analyzed by comparing the chronoamperometric curves to the dimensionless theoretical curves for the diffusion-controlled nucleation and growth of crystals in three dimensions (3D) proposed by Scharifker and Hills (SH) [18].

The expressions for the instantaneous and progressive nucleation with 3D growth are given by following equations [21],

$$i^2/i^2_{\max} = 1.9542[t_{\max}/t]\,\{1 - \exp[-1.2564t/t_{\max}\}^2 \quad (1)$$

$$i^2/i^2_{\max} = 1.2254[t_{\max}/t]\left\{1 - \exp[-2.3367(t/t_{\max})^2\right\}^2 \quad (2)$$

where $i_{\max}$ and $t_{\max}$ are the maximum current density observed at the maximum time $t_{\max}$ [22].

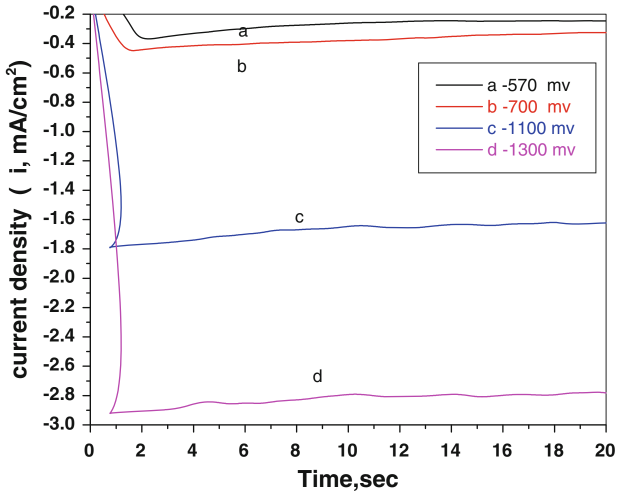

Fig. 2 Potentiostatic (I–t) transients for nucleation and growth of (NiZn)Fe_2 alloy at *a* −570 mV, *b* −700 mV, *c* −1100 mV, *d* −1300 mV

The fitting of the experimental curves for the theoretical curves were shown in Fig. 3a–d. The curves indicated that the nucleation and growth of Ni–Zn–Fe alloy electrodeposited from ethylene glycol followed instantaneous mechanism.

Electrodeposition of (NiZn)Fe_2 alloy

According to Matloz [24], reduction of divalent cations, Ni(II), Zn (II) and Fe(II), is a two-step process where it first takes up one electron to make monovalent adsorbed cations Ni(I)ads, Fe(I)ads and Zn(I)ads and then the second electron takes it to deposited neutral atom. Hydrogen evolution due to reduction of protons and dissociation of ethylene glycol molecule were considered as side reactions [15]. Side reactions reduced the current efficiency and the kinetics of metals reduction. Table 1 showed the conditions used for the electrodeposition of (NiZn)Fe_2 alloy on copper substrate.

The current efficiency of the Ni–Zn–Fe alloy deposition was calculated by using the simple relation:

$$\varphi = 100 \times \left(m_{\text{exp}}/m_{\text{th}}\right) \quad (3)$$

where m_{exp} and m_{th} are the experimental and theoretical masses of the (NiZn)Fe_2 alloy which was represented in Fig. 4. The theoretical mass of Ni–Zn–Fe alloy (m_{th}) can be calculated according to Faraday's law [15]. The effect of current density on current efficiency was studied to get the highest efficiency as shown in Table 2 and Fig. 5.

It can be noticed that the current efficiency was increased initially with the increase in the current density to 153 mA cm^{-2}. The current efficiency ~67.6% was obtained and then decreased with the increase of current density within the range studied. At current densities less than 153 mA cm^{-2}, the metals deposition rates were relatively low leading to low current efficiency. Further, increasing in the current density than 153 mA cm^{-2} was associated with the increase in the dissociation rate of ethylene glycol molecules that caused the hydrogen evolution to be the dominant reaction on the cathode. This was accompanied with the decrease in the current efficiency [15, 16].

Anodization of the (NiZn)Fe_2 alloy

Electrochemical oxidation of (NiZn)Fe_2 alloy films prepared at the optimum electrodeposition synthesis parameters was carried out at room temperature (25 °C) according to the conditions summarized in Table 3.

The conversion of MFe_2 alloy to the corresponding ferrite (MFe_2O_4) via the hydroxide form can be explained with the following reaction:

$$MFe_2 + 8OH^- \rightarrow MFe_2O_4 + 4H_2O + 8e^- \quad (4)$$

After oxidation, the hydroxide films were washed with deionized water and preserved in desiccator. Then,

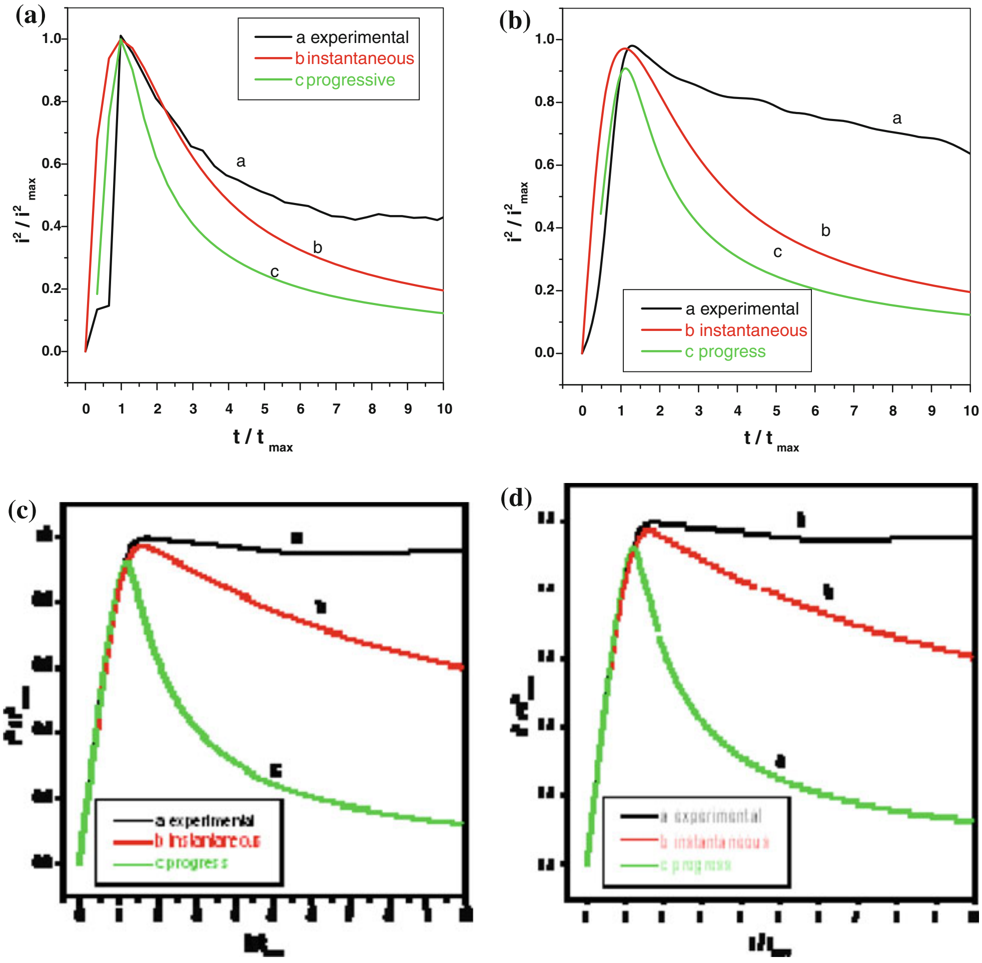

Fig. 3 Nondimensional i^2/i^2_{max} vs t/t_{max} plots for electrodeposited (NiZn)Fe$_2$ alloy at different potentials **a** −570 mV, **b** −700 mV, **c** −1100 mV, **d** −1300 mV)

Table 1 Conditions used for synthesis of (NiZn)Fe$_2$ alloy from ethylene glycol sulphate

Electro deposition	
Bath composition	5 mL 0.1 M ZnSO$_4$ + 5 mL 0.1 M NiSO$_4$ + 20 mL 0.1 M (NH$_4$)$_2$Fe(SO$_4$)$_2$ + 10 mL 0.1 M citric acid + 2 g NaCl)
Current density (mA/cm^2)	52, 102, 153, 204
Deposition time (min)	180
Bath temperature (°C)	25
Substrate	Cu(BDH)
Stirring (rpm)	800

annealing of the hydroxide converted into the corresponding oxide (ferrite) should remove some of the defects, which may be presented during the electrodeposition and anodization steps, such as voids, grain boundaries, dislocations, stresses, in homogeneity, etc. Thus, annealing is a process related to the stress relief and local structural rearrangements resulting in recovery of stoichiometry in the film [15]. The formed (NiZn)Fe$_2$ hydroxide precursors were annealed at 850 °C for 4 h. After annealing, a sharper and more intense diffraction peak due to the (311) plane (expected for spinel structure) is observed. This observation suggested that the nucleation of a spinel phase was formed after anodization and the crystallization process was completed after annealing [15].

The effect of variation of nickel zinc ratios and its impact on the properties of the ferrite powders Ni$_x$Zn$_{1-x}$Fe$_2$O$_4$ was studied. Series of experiments were carried out at Ni molar ratio from 0.4 to 0.9 annealed at 850 °C for 4 h and the results were confirmed by XRD patterns given in Fig. 6. The results ascribed that confirmed the presence of

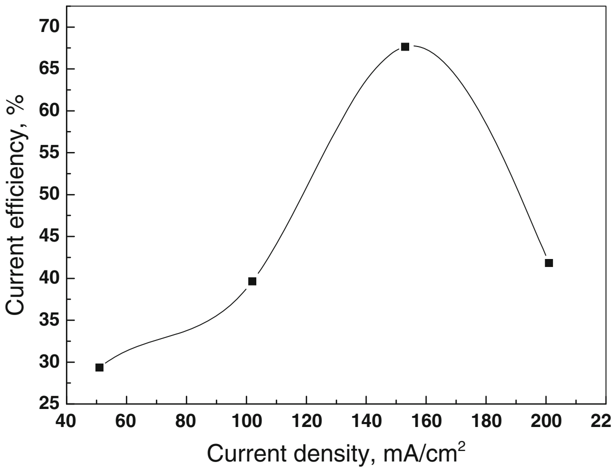

Fig. 4 Variation of current efficiency with current density for (NiZn)Fe_2 alloy

Table 2 Effect of current density of electrodeposited (NiZn)Fe_2 on current efficiency

Current density(mA/cm^2)	Current efficiency %
52	29.3
102	39.6
153	67.6
204	41.8

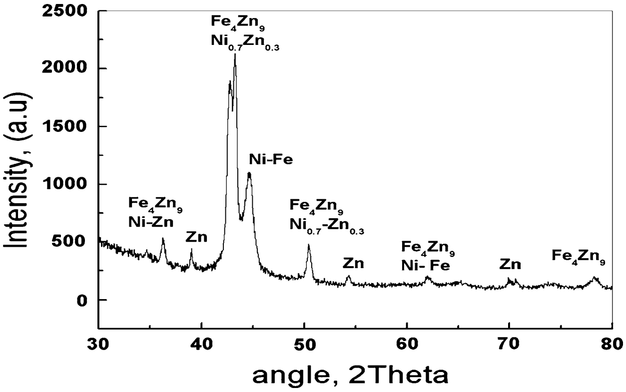

Fig. 5 XRD patterns of (NiZn)Fe_2 alloy electrodeposited from ethylene glycol sulphate bath at current density 153 mA/cm^2

Table 3 Conditions of the anodization process for the synthesis of nickel–zinc ferrites thin films

Items	Conditions
Electrolyte	1 M KOH
Current density (mA/cm^2)	20
Intercalation time (min)	40
Electrolyte temperature (°C)	25

cubic structure of $Ni_xZn_{1-x}Fe_2O_4$ phase (JCPDS# 08-0234). Secondary phase of hematite α-Fe_2O_3 (JCPDS# 73-603) was formed as impurity with the produced spinel $Ni_xZn_{1-x}Fe_2O_4$ ferrites with the increase of Ni^{2+} molar ratio up to 0.6. The hematite formation is a consequence of the preferential loss of one or more divalent cation during the deposition conditions [21].

The crystallite sizes for the most intense peak (311) plane at 2θ value of 35.4 were estimated from XRD data using Debye–Scherrer formula. Table 4 showed the changes of $Ni_xZn_{1-x}Fe_2O_4$ ferrites and the crystallite size with the substitution of Ni^{2+} molar ratios. The crystallite size for the produced ferrite increased with increasing nickel content, from 59 nm at Ni ($x = 0.2$) to 81 nm at Ni ($x = 0.6$) then decreased with the Ni molar ratio from 0.6 to 0.9. The decrease in crystalline size can be attributed to the presence of α-Fe_2O_3 causing shrinkage of the lattice [25].

The microstructures of the produced films investigated by SEM micrographs are showed in Fig. 7a, b. The SEM micrographs of $Ni_{0.5}Zn_{0.5}Fe_2O_4$ films in Fig. 7a were appeared as the agglomerated spherical particles in laminate shape. Increasing the Ni mole ratio to 0.9 as represented in Fig. 7b showed the presence of fines spheres with pseudo-cubic like structure related to the presence of α-Fe_2O_3 phase with the spinel ferrite phase.

The magnetization of the produced $Ni_xZn_{1-x}Fe_2O_4$ thin films annealed at 850 °C for 4 h was measured under an applied field of 15 kOe at room temperature. The *M*–*H* hysteresis loops were given in Fig. 8 and the magnetic parameters were summarized in Table 4.

It can be seen that the saturation magnetization M_s was increased linearly to maximum value of 48.8 emu/g at Ni content ($x = 0.5$) and then decreased with further addition

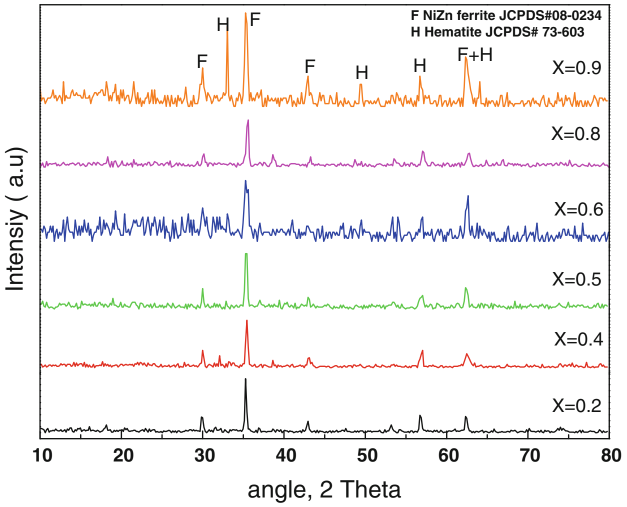

Fig. 6 XRD patterns of the produced $Ni_xZn_{1-x}Fe_2O_4$ films at different Ni molar ratios from 0.2 to 0.9 annealed at 850 °C for 4 h

Table 4 Effect the nickel content on the crystallite size and the magnetic properties of $Ni_xZn_{1-x}Fe_2O_4$ thin film

Composition	x	Hematite percent	Crystal size (nm)	Magnetic properties		
				M_s (emu/g)	M_r (emu/g)	H_c (Oe)
$Ni_{0.2}Zn_{0.8}Fe_2O_4$	0.2	–	59	21.6	1.4	4.5
$Ni_{0.4}Zn_{0.6}Fe_2O_4$	0.4	–	81.4	43.1	3.8	11.1
$Ni_{0.5}Zn_{0.5}Fe_2O_4$	0.5	–	62.4	48.8	4.9	14.9
$Ni_{0.6}Zn_{0.4}Fe_2O_4$	0.6	3	81.4	46.6	9.2	68.5
$Ni_{0.8}Zn_{0.2}Fe_2O_4$	0.8	6.3	64.4	36.6	7.4	79.4
$Ni_{0.9}Zn_{0.1}Fe_2O_4$	0.9	15	32.8	36.3	6.5	92.2

of Ni^{2+} ions. The changes in saturation magnetization may be attributed to changes in Ni and Zn concentrations in the spinel lattice. The Ni^{2+} ions have a marked preference for octahedral sites because of their favourable fit of charge distribution of this ion in the crystal field of the octahedral site. On other hand, Zn^{2+} ions have preference for the tetrahedral site. Then at low Ni content, the migration of Fe^{3+} ions from A- to B-sites is increased with increasing Zn content to accommodate the increased number of Zn ions on A-sites as per their site preference. This migration results in an increase in Fe^{3+} concentration on B-sites which gives rise to antiparallel spin coupling and spin canting resulting in weakening of the A–B exchange interaction reducing thereby the magnetization [26–28]. Moreover, the presence of the nonmagnetic α-Fe_2O_3 species led to decrease the saturation magnetization at high Ni molar ratios from 06 to 0.6. The coercivity H_c was increased with the size until it reached 68.4 Oe at Ni molar ratio ($x = 0.6$). With the further increase in the nickel content, the coercivity was increased, although the crystallite size was decreased. The maximum value of coercive force was ($H_c = 92.1$ Oe) at Ni content ($x = 0.9$). This was attributed to the enhanced role of the surface and its strong anisotropy, as opposed to the weaker bulk anisotropy [27]. Moreover, the increase in the coercive force might be related to the residual α-Fe_2O_3 having a high intrinsic coercive force [29].

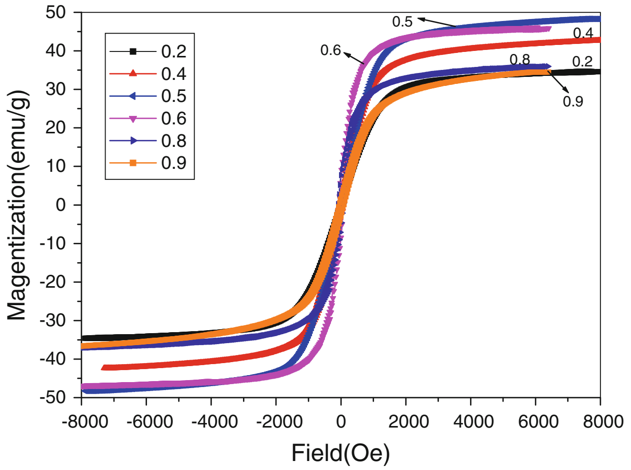

Fig. 8 Effect of Ni concentration on *M–H* hysteresis loop of $Ni_xZn_{1-x}Fe_2O_4$ thin films with x varying from 0.2 to 0.9

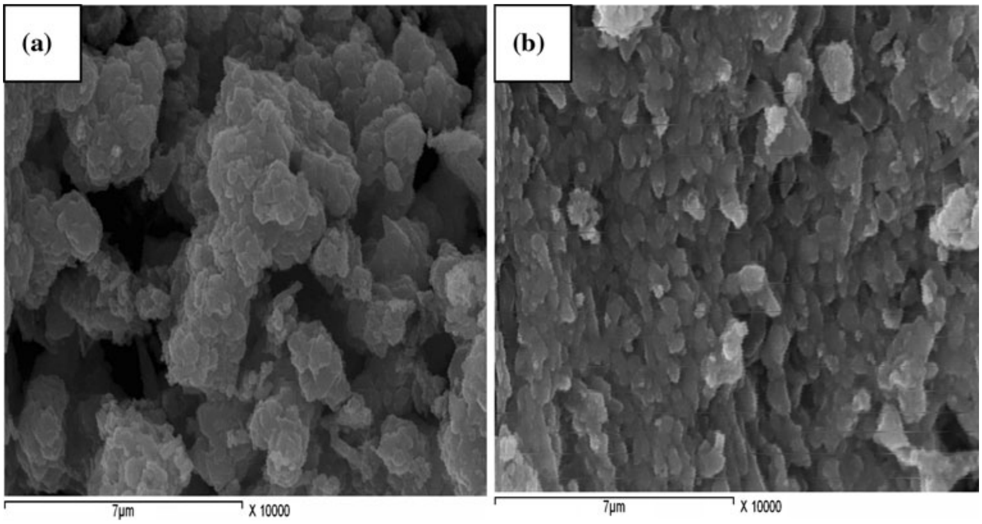

Fig. 7 SEM images of $Ni_xZn_{1-x}Fe_2O_4$ thin films with Nickel molar ratio x (**a** 0.5, **b** 0.9) annealed at 850 °C for 4 h

The XRD patterns of Ni–Zn ferrites films annealed at 850 °C for different times from 1 to 4 h were shown in Fig. 9. The intensities of the peaks were increased with increasing the annealing time. This indicated that the crystallinity of the products was improved with the annealing time. The integral intensity of the (311) peak I_x of the spinel Ni–Zn ferrite phase was calculated by measuring the area under the curve [30].

The intensity of the (311) peak I_A of the powder obtained after annealing for 4 h was used as a standard of crystallization, because no increase in the intensity of the peak after 4 h was observed. I_x was the intensity of (311) peak at time t, the fraction of crystallization in the reactive system can be calculated by the formula of $x = I_x/I_A$. Isothermal crystallization can be described by the Avrami transformation kinetic equation [30, 31]

$$x = 1 - \exp(-kt^n) \tag{5}$$

where n is Avrami exponent (constant), depending on the details of the nucleation and growth mechanisms, x is the fraction of crystallization, k is reaction rate constant and t is reaction time. For isothermal condition,

$$\ln[-\ln(1-x)] = \ln K + n\ln t \tag{6}$$

Plotting of ln [−ln (1 − x)] as a function of ln t yields the values of n as shown in Fig. 10. The straight line obtained showed the mechanism of the crystallization is a random nucleation, with nucleation as the rate-determining step, could be applied. For this system, the rate of crystallization is controlled by the nucleation in an assemblage of identical; reactant fragments and the first-order expression are obeyed in random nucleation, as follows [31]:

$$\mathrm{d}x/\mathrm{d}t = k(1-x) \tag{7}$$

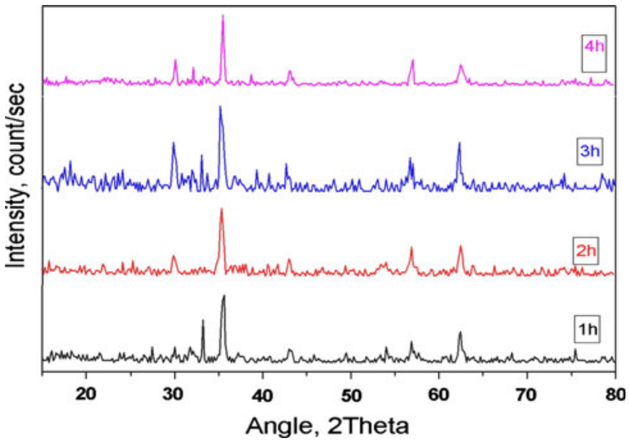

Fig. 9 XRD patterns of the produced $Ni_{0.5}Zn_{0.5}Fe_2O_4$ film annealed at 850 °C for different times from 1 to 4 h

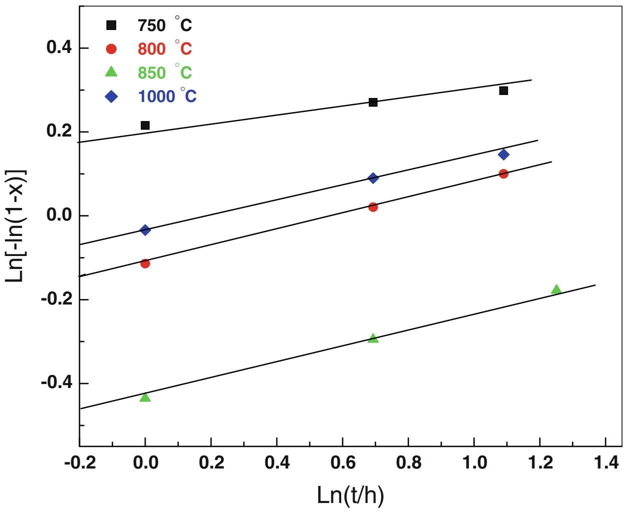

Fig. 10 Avrami plot of ln [−ln (1 − x)] vs. ln t for isothermal crystallization of $Ni_{0.5}Zn_{0.5}Fe_2O_4$ films annealed at different temperatures from 750 to 1000 °C for different times from 1 to 4 h

$$-\ln(1-x) = kt \tag{8}$$

The temperature dependence of k in Eq. 7 could be described as a simple Arrhenius behaviour, i.e.

$$k = v\exp\{-E/(RT)\} \tag{9}$$

where v is the frequency factor, E is the apparent activation energy of crystallization and R is the gas constant. Taking logarithms of Eq. 9

$$\ln k = \ln v - (E/RT) \tag{10}$$

By plotting the ln k values versus the reciprocal of absolute temperature Arrhenius plot was obtained. The slope of $-E/R$, the activation energy of crystallization calculated, was found to be 62 KJ/mol as shown in Fig. 11. This value was

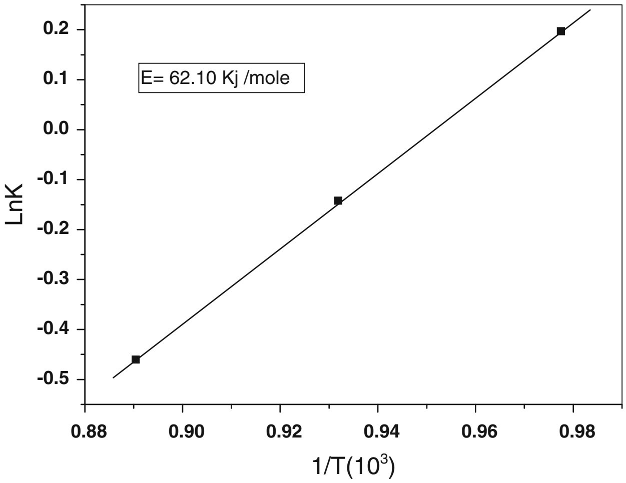

Fig. 11 Arrhenius plots of ln k values against the reciprocal of the temperature for determination the activation energy of $Ni_{0.5}Zn_{0.5}Fe_2O_4$ films formed by electrochemical processing

higher than the value obtained by Wang and Kung that used the hydrothermal process for synthesis of Ni–Zn ferrites nanoparticles [31], representing that the electrochemical technique can give good stable ferrites.

Conclusions

The results can be summarized as follows:

- Ni–Zn ferrites have been successfully synthesized via a novel approach of electrodeposition–anodization process.
- Electrodeposited (NiZn)Fe_2 alloy was formed from non-aqueous ethylene glycol sulphate bath at current density 153 mA/cm^2 with high current efficiency 67.7%.
- The formed alloy was anodized in 1 M KOH to form nickel–zinc ferrites precursors which annealed at 850 °C for 4 h.
- The results revealed that single phase of $Ni_xZn_{1-x}Fe_2O_4$ ferrite was obtained with nickel substitution from 0.2 to 0.5 whereas increase in nickel substitution up to 0.6 led to formation of α-Fe_2O_3 as impurity phase.
- The crystallite size of the formed films was in the range from 32.8 to 81.4 nm.
- The microstructure of the produced $Ni_{0.5}Zn_{0.5}Fe_2O_4$ films was appeared as the laminate-like structure.
- High saturation magnetization ($M_s = 48.8$) was achieved for $Ni_{0.5}Zn_{0.5}Fe_2O_4$ phase annealed at 850 °C for 4 h.
- The crystallization of Ni–Zn ferrite was approached to be first-order reaction and the activation energy was found to be 62 KJ/mol.

References

1. Ghazanfar U (2005) PhD thesis, Punjab University, Pakistan
2. Upadhyay C, Mishra D, Verma HC, Anand S, Das RP (2003) J Magn Magn Mater 260:188
3. Silo EE, Rotelo R, Jacobo SE (2002) Phys B 320:257
4. Ravinder D, Kumar KV, Reddy AVR (2003) Mater Lett 57:412
5. Sorescu M, Diamandescu L, Swaminathan R, McHenry ME, Feder M (2005) J Appl Phys 97:10G105
6. Yang Z-h, Gong Z-q, Li H-x, Ma Y-t, Yang Y-f (2006) J Cent South Univ Technol 6:618
7. Banerjee M, Verma N, Prasad R (2007) J Mater Sci 42:1833. doi:10.1007/s10853-006-0821-1
8. Rosales MI, Cuautle MP, Castano VM (1998) J Mater Sci 33:3665. doi:10.1023/A:1004671732746
9. Takayama A, Kondo K, Okuya M, Kaneko S (2002) J Ceram Soc Jpn 110:916
10. Thakur S, Katyal SC, Singh M (2009) J Magn Magn Mater 321:1
11. Washburn C, Jorne J, Kurinec S (2006) Key Eng Mater 314:127
12. Roy MK, Verma HC (2006) J Magn Magn Mater 306:98
13. Nuli Y-N, Qin QZ (2005) J Power Sources 142:292
14. Lokhande CD, Kulkarni SS, Mane RS, Han S-H (2007) J Cryst Growth 303:387
15. Sartale SD, Lokhande CD, Muller M (2003) Mater Chem Phys 80:120
16. Satale SD, Lokhande CD, Giersig M, Ganesan V (2004) J Phys Condens Matter 16:773
17. Gómez E, Pané S, Vallés E (2005) Electrochem Commun 7:1225
18. Ballesteros JC, Arista PD, Meas Y, Ortega R, Trejo G (2007) Electrochim Acta 52:3686
19. Miranda FJF, Barcia OE, Diaz SL, Mattos OR, Wiart R (1996) Electrochim Acta 41:1041
20. Diaz SL, Mattos OR, Barcia OE, Miranda FJF (2002) Electrochim Acta 47:4091
21. Yin K-M, Lin B-T (1996) J Surf Coat Technol 78:205
22. Inamdar AI, Mujawar SH, Sadale SB, Sonavane AC, Shelar MB, Shinde PS, Patlil PS (2007) Sol Energy Mater Sol Cells 91:864
23. Yang ZN, Zhang Z, Zhang JQ (2006) J Surf Coat Technol 200:4810
24. Matlosz M (1993) J Electrochem Soc 140:2272
25. Sheikh AD, Mathe VL (2008) J Mater Sci 43:2018. doi:10.1007/s10853-007-2302-6
26. Verma A, Chatterjee R (2006) J Magn Magn Mater 306:313
27. Rashad MM, Elsayed EM, Moharam MM, Abou-Shahbab RM, Saba AE (2009) J Alloys Compd 486:759
28. Hessien MM, Rashad MM, El-Barawy K, Ibrahim IA (2008) J Magn Magn Mater 320:1615
29. Hessien MM, Rashad MM, El-Barawy K (2008) J Magn Magn Mater 320:336
30. Z-Hui Y, Qing GZ-, Xu LH-, Tian MY-, Fang YY- (2006) J Cent South Univ Technol 13:618
31. Wang HW, Kung SC (2004) J Magn Magn Mater 270:230